

# Chapter 2

## Component Optimization of Sb–Te for Ti–Sb–Te Alloy

### 2.1 Ti-Doped Sb<sub>2</sub>Te Alloy

#### 2.1.1 Introduction

Phase-change memory (PCM) has been considered to be one of the best candidates for a so-called storage class memory (SCM) due to its nonvolatile nature, high scalability, fast operation speed, and high endurance [1–3]. For replacing Flash by SCM, good data retention is required while write speed below 10 ns is needed for substituting DRAM [4]. However, Ge<sub>2</sub>Sb<sub>2</sub>Te<sub>5</sub> (GST), the most researched phase-change material, shows an unsatisfied data retention of 85 °C@10-year and low crystallization speed of 100 ns [5, 6]. Although N, [7, 8] C, [9, 10] and SiO<sub>2</sub> [11, 12]-doped GST can improve the thermal stability of amorphous state, the crystallization speed is slowed. Meanwhile, Sn, [13, 14] Bi [15, 16]-doped GST accelerates the operation speed while impact negatively on the data retention. The trade-off between data retention and operation speed makes the application of GST-based PCM as SCM very difficult to achieve. What's more, the relatively high melting point (620 °C) of GST leads to high Reset current of GST-based PCM, which limits the PCM scaling capability [17].

For these reasons, new phase-change materials are needed. It is well known that growth-dominated phase-change materials possess a fast crystallization speed than nucleation-dominated ones (such as GST), which is easier to meet the requirement of high operation speed. In addition, since the Reset operation needs to melt the phase-change materials, phase change materials with low melting temperature ( $T_m$ ) are very beneficial for reducing Reset current and energy consumption. As famous growth-dominated phase-change materials, Sb–Te binary alloys, which are widely applied in phase-change optical recording, show faster crystallization speed than GST [18]. From the Sb–Te phase diagram, as shown in Fig. 2.1, we can find that there are three equilibrium phases:  $\delta$ ,  $\gamma$ , and Sb<sub>2</sub>Te<sub>3</sub> [19]. Among the three

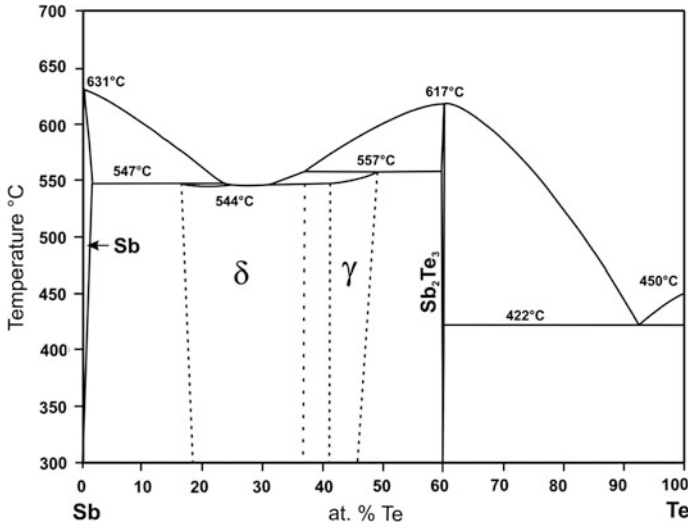


**Fig. 2.1** Phase diagram of Sb–Te alloys. These alloys have three equilibrium phases:  $\delta$ ,  $\gamma$ , and  $\text{Sb}_2\text{Te}_3$ . Among these three phases,  $\delta$  phase has the lowest melting point (544 °C) [20]

equilibrium phases,  $\delta$  phase exhibits the lowest  $T_m$  (only 544.1 °C), which seems to be a good choice.  $\delta$  phase forms by peritectic reactions  $L (\text{liquid}) + (\text{Sb}) \leftrightarrow \delta$ , [20] and Te concentration ranges from 16.5 at. to 37 at.%. It is worth considering that the crystallization rate of Sb–Te alloys is proved to be enhanced by increasing Sb/Te ratio [18]. In addition, Sb–Te alloy with 33 at. % Te ( $\text{Sb}_2\text{Te}_3$ ) has been widely used in CD after incorporating with Ag and In. Thus,  $\text{Sb}_2\text{Te}_3$  is chosen in this work to accelerate the crystallization speed.

Although  $\text{Sb}_2\text{Te}_3$  (ST) has high crystallization speed and low  $T_m$ , its poor thermal stability makes it not suitable for being used directly in PCM, which is a common drawback in Sb-rich Sb–Te alloys [21]. In order to obtain high data retention, doping seems to be essential. However, the dopant is rigorous: on the one hand, the thermal stability should be significantly improved after doping. On the other hand, the fast crystallization speed of ST would not be greatly affected. Furthermore, for getting good endurance, phase separation is better to be avoided. Previous researches show that, in the thermoelectric field, Ti atoms can replace parts of Sb atoms in  $\text{Sb}_2\text{Te}_3$  owing to smaller covalent radii ( $r_{\text{Ti}} = 0.132 \text{ nm}$ ,  $r_{\text{Sb}} = 0.140 \text{ nm}$ ) [22, 23]. The structure of  $\text{Sb}_2\text{Te}_3$  can be described by periodically stacked Sb–Te (the structure of  $\text{Sb}_2\text{Te}_3$ ) and Sb layers [24]. Based on the similar structure of  $\text{Sb}_2\text{Te}_3$  and  $\text{Sb}_2\text{Te}_3$ , we have reason to believe that Ti atoms will be substitutional atoms in Ti-doped ST. Therefore, in this work, Ti was incorporated in  $\text{Sb}_2\text{Te}_3$  for getting good data retention and fast crystallization rate. Crystal structure, thermal stability, and device performance of TST were studied.

### 2.1.2 Experimental Section

Ti<sub>10</sub>Sb<sub>60</sub>Te<sub>30</sub> films were deposited by the cosputtering of Ti and Sb<sub>2</sub>Te targets on SiO<sub>2</sub>/Si substrates using a RF sputtering system at room temperature. Pure Sb<sub>2</sub>Te and Ti films were also prepared for comparison. Thermal stability of the amorphous films was studied by in situ time-dependent resistance measurement at various isothermal annealing temperatures in the range of 195–210 °C. Crystal structures of Sb<sub>2</sub>Te and Ti<sub>10</sub>Sb<sub>60</sub>Te<sub>30</sub> films annealed at 250 °C were investigated by X-ray diffraction (XRD) with Cu  $K\alpha$  radiation ( $\lambda = 1.54056$  Å). X-ray photoelectron spectroscopy (XPS) measurement with Al  $K\alpha$  radiation was used to confirm the element-binding situation of pure Ti, crystalline Sb<sub>2</sub>Te and Ti<sub>10</sub>Sb<sub>60</sub>Te<sub>30</sub> films. High-resolution electron microscopy (HRTEM) study was carried out to observe the morphology and microstructure. T-shaped PCM test cell with a tungsten-heating electrode 190 nm in diameter has been fabricated using 0.13  $\mu$ m CMOS technology. Between the top electrode and Ti<sub>10</sub>Sb<sub>60</sub>Te<sub>30</sub> phase-change film (50 nm), 20 nm-thick TiN film was deposited. The resistance–voltage and programming cycle tests were measured by a Keithley 2400C and a Tektronix AWG5002B pulse generator.

### 2.1.3 Thermal Stability

The sheet resistances ( $R_s$ ) of Sb<sub>2</sub>Te and Ti<sub>10</sub>Sb<sub>60</sub>Te<sub>30</sub> films as a function of the annealing temperature ( $R$ - $T$ ) are shown in Fig. 2.2a. For Sb<sub>2</sub>Te film, a sudden  $R_s$  drops at about 139 °C is clearly observed after a continuous and slow decrease. The drop of  $R_s$  reflects the phase transition from the amorphous state to the crystalline state. The crystallization temperature of Ti<sub>10</sub>Sb<sub>60</sub>Te<sub>30</sub> increases to 211 °C, which

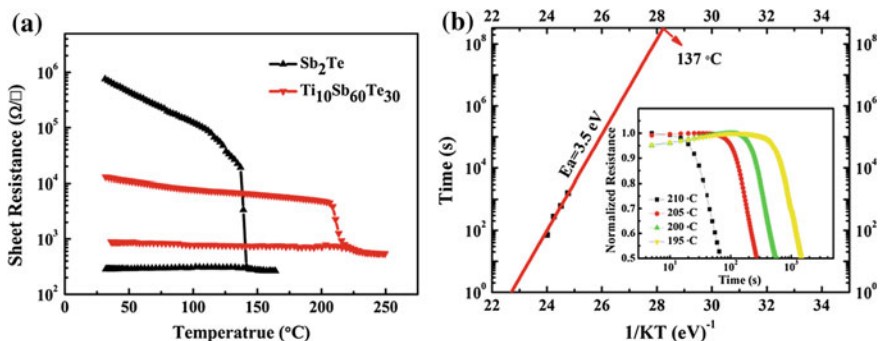


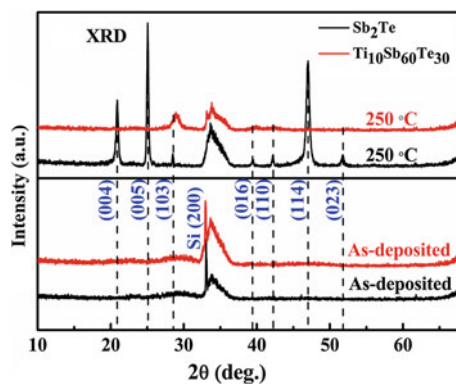
**Fig. 2.2** **a** Sheet resistance as a function of temperature for Sb<sub>2</sub>Te and Ti<sub>10</sub>Sb<sub>60</sub>Te<sub>30</sub> films. **b** The Arrhenius extrapolation @10-year of data retention for Ti<sub>10</sub>Sb<sub>60</sub>Te<sub>30</sub> film. The inset shows normalized sheet resistance as a function of time at various isothermal annealing temperatures

means that thermal stability of the amorphous state will be remarkably improved. It is worth pointing out that crystalline  $R_s$  of  $\text{Ti}_{10}\text{Sb}_{60}\text{Te}_{30}$  is increased. The improved  $R_s$  value implies that a lower power is needed to achieve the phase transition from the crystalline phase to the amorphous phase. Figure 2.2b presents data retention characteristics for  $\text{Ti}_{10}\text{Sb}_{60}\text{Te}_{30}$  films. Low failure-time is obtained with high annealing temperature. By extrapolation from the failure-time to ten years, based on the Arrhenius law, a 10-year lifetime temperature of 137 °C for  $\text{Ti}_{10}\text{Sb}_{60}\text{Te}_{30}$  film is provided, with activation energy  $E_a$  of 3.5 eV. These results are much better than those of  $\text{Sb}_2\text{Te}$  (33 °C for 10 years with  $E_a$  of 1.7 eV [25]) and conventional GST (85 °C for 10 years with  $E_a$  of 2.2 eV [5]). Besides, the thermal stability even can satisfy the requirements of automotive systems.

### 2.1.4 Crystalline Structure

In order to explain the good thermal stability of  $\text{Ti}_{10}\text{Sb}_{60}\text{Te}_{30}$  film, XRD was applied to investigate the structure of  $\text{Ti}_{10}\text{Sb}_{60}\text{Te}_{30}$  films. Figure 2.3 shows the XRD results for  $\text{Sb}_2\text{Te}$  and  $\text{Ti}_{10}\text{Sb}_{60}\text{Te}_{30}$  films. Both as-deposited films show no diffraction peak, which indicates that  $\text{Ti}_{10}\text{Sb}_{60}\text{Te}_{30}$  film is still in the amorphous state. Diffraction peaks of the hexagonal phase are observed in  $\text{Sb}_2\text{Te}$  film annealed at 250 °C. The diffraction peaks of  $\text{Ti}_{10}\text{Sb}_{60}\text{Te}_{30}$  film, in comparison to  $\text{Sb}_2\text{Te}$  film, show a decrease in the intensity, some of them even disappearing, and a shift to larger angle in the diffraction angle. No new phase forms in the  $\text{Ti}_{10}\text{Sb}_{60}\text{Te}_{30}$  film. The broad diffraction peaks imply that the crystalline process of  $\text{Sb}_2\text{Te}$  is inhibited remarkably by incorporation Ti. Hence,  $\text{Ti}_{10}\text{Sb}_{60}\text{Te}_{30}$  film is probably in a nano-crystalline phase. The movement of the peaks is due to the decrease in the lattice parameters [26]. It has reported that Ti atoms will replace part of Sb atoms in Ti–Sb–Te alloys, accompanying with a decrease of lattice constant as a result of smaller ionic radii of Ti ( $r_{\text{Ti}} = 0.132$  nm,  $r_{\text{Sb}} = 0.140$  nm).

**Fig. 2.3** X-ray diffraction patterns of  $\text{Sb}_2\text{Te}$  and  $\text{Ti}_{10}\text{Sb}_{60}\text{Te}_{30}$  films.  $\text{Ti}_{10}\text{Sb}_{60}\text{Te}_{30}$  has a similar structure as  $\text{Sb}_2\text{Te}$



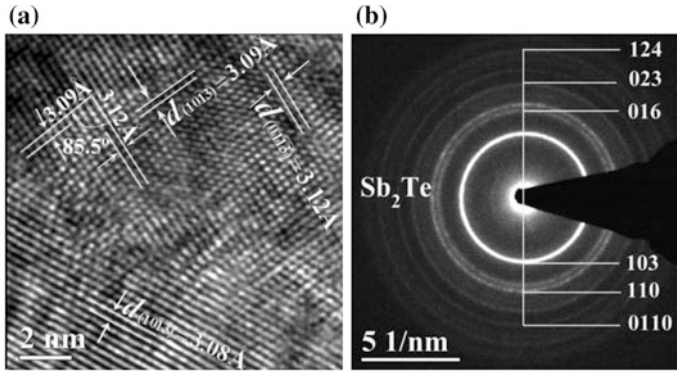


**Fig. 2.4** The HRTEM image **a** and SAED patterns **b** of Ti<sub>10</sub>Sb<sub>60</sub>Te<sub>30</sub> film annealed at 250 °C. Ti<sub>10</sub>Sb<sub>60</sub>Te<sub>30</sub> film is in polycrystalline state with {1 0 3} preferential orientation

The microstructure of Ti<sub>10</sub>Sb<sub>60</sub>Te<sub>30</sub> film annealed at 250 °C was characterized through HRTEM image and selected area electron diffraction (SAED) patterns, as shown in Fig. 2.4. In the HRTEM image, the Ti<sub>10</sub>Sb<sub>60</sub>Te<sub>30</sub> film is completely crystallized into nano-crystalline grains. Spacing of the lattice fringes are calculated to be 3.08, 3.09, and 3.12 Å, which are close to the interplanar distance of {0 1 3} planes of hexagonal phase Sb<sub>2</sub>Te (3.13 Å). Besides, the included angle of the last two lattice fringes is 85.5°, which is in good agreement with the included angle between (10 $\bar{1}$ 3) and (01 $\bar{1}$ 3) planes (85.7°). Therefore, all crystalline phases in the HRTEM image are belonging to the hexagonal phase Sb<sub>2</sub>Te. SAED patterns in Fig. 2.4b exhibit polycrystalline rings, which are well indexed as hexagonal phase Sb<sub>2</sub>Te with 1 0 3 preferential orientations, consistent well with the XRD result. The continuity of these diffraction rings also proves the nano-crystalline structure of Ti<sub>10</sub>Sb<sub>60</sub>Te<sub>30</sub> film with small grain size. HRTEM image and SAED patterns further confirm that there is no new phase formed in Ti<sub>10</sub>Sb<sub>60</sub>Te<sub>30</sub> film, which is very beneficial for the reliability of PCM device.

### 2.1.5 Device Performance

Possessing a high crystallization temperature of 211 °C and good data retention of 10-year @ 137 °C, Ti<sub>10</sub>Sb<sub>60</sub>Te<sub>30</sub> is expected to keep good reversible phase-change ability. Figure 2.5a shows the typical current–voltage (*I*–*V*) characteristics of Ti<sub>10</sub>Sb<sub>60</sub>Te<sub>30</sub>-based PCM device. Starting from the amorphous phase, a high nonohmic resistivity is exhibited and voltage increases sharply with the rising current. Further increasing the current to a certain value, the voltage suddenly drops, and the material switches rapidly from amorphous state (Reset state) into a highly conductive state (Set state), displaying an S-shaped negative differential conductivity. Figure 2.5b shows typical resistance–voltage (*R*–*V*) curves for the

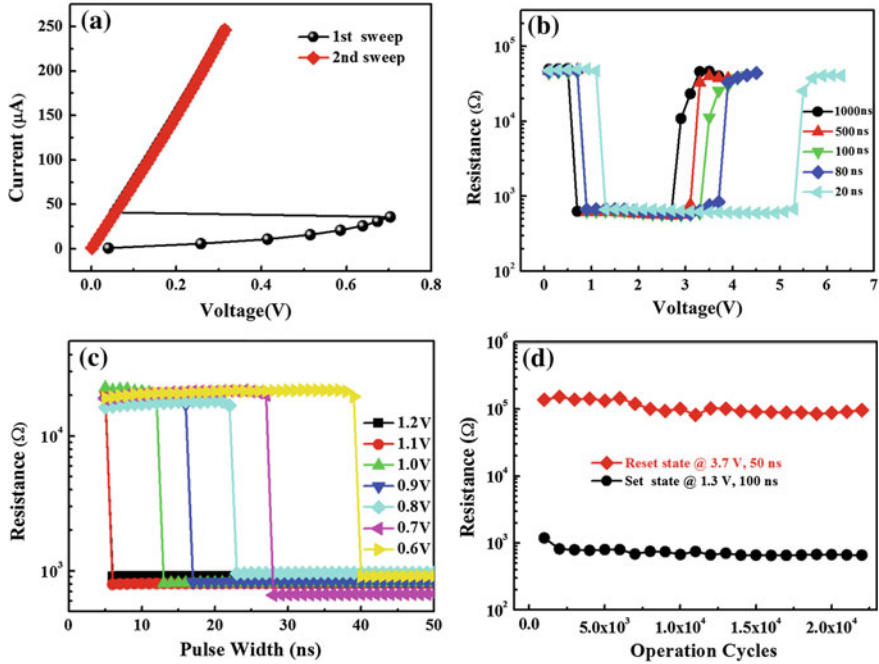


**Fig. 2.5** **a** Current–voltage and **b** Resistance–voltage characteristics of  $\text{Ti}_{10}\text{Sb}_{60}\text{Te}_{30}$ -PCM device. **c** Resistance of the device as a function of pulse width at different fixed pulse amplitudes. **d** The endurance characteristic of the device

PCM cell with different pulse widths. Owing to less energy produced by narrower pulse, the Set and Reset voltages for different pulse widths are distinguishing. For 1000 ns electric pulse, a complete crystallization is easily achieved with a Set voltage of 0.7 V and a Reset voltage of 3.3 V for re-amorphization. It is worth noting that the device still can achieve Set and Reset operations with 20 ns pulse, although a higher Reset voltage is required. Another prominent characteristic of the device is that the  $\text{Ti}_{10}\text{Sb}_{60}\text{Te}_{30}$  can crystallize completely regardless of pulse length while, in the case of GST, the Set resistance value is much more sensitive to pulse length and amplitude [27].

Operation speed is another important parameter for PCM applications, which is almost determined by crystallization speed. The required time for Set ( $t_{\text{Set}}$ ) operation was measured as a function of applied pulse widths with different amplitudes, as shown in Fig. 2.5c. When the pulse voltage is fixed at 0.6 V, the device transitions from the high resistance state to a low resistance state as pulse width exceeds 40 ns. The change of  $t_{\text{Set}}$  is regular with the increase of pulse amplitude: the higher voltage is, the lower  $t_{\text{Set}}$  is needed. Remarkably, the  $t_{\text{Set}}$  decreases to 6 ns as the voltage larger than 1.1 V. What is more, under fixed pulse amplitude, the device resistances of amorphous and polycrystalline states are very stable with good repeatability. The experimental result demonstrates that

Ti<sub>10</sub>Sb<sub>60</sub>Te<sub>30</sub>-based PCM cell has extremely rapid operation speed. Figure 2.5d shows the endurance of Ti<sub>10</sub>Sb<sub>60</sub>Te<sub>30</sub>-based PCM cell. Endurance up to  $2 \times 10^4$  cycles is demonstrated, where applied Set and Reset pulses are just 100 and 50 ns, respectively.

### 2.1.6 Summary

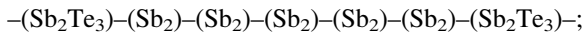
In this work, Ti is proposed to be incorporated into the Sb<sub>2</sub>Te phase-change material to break the conflict between thermal stability and operation speed of PCM. With high crystallization temperature of 211 °C and good data retention of 137 °C for 10 years, Ti<sub>10</sub>Sb<sub>60</sub>Te<sub>30</sub> is found to have much better thermal stability than usual GST. Meanwhile, Ti<sub>10</sub>Sb<sub>60</sub>Te<sub>30</sub>-based PCM device shows good reversible phase-change ability and fast crystallization speed as short as 6 ns. XRD and HRTEM results demonstrate that hexagonal Sb<sub>2</sub>Te is the only phase exists in the crystalline Ti<sub>10</sub>Sb<sub>60</sub>Te<sub>30</sub>.

## 2.2 Ti-Doped Sb<sub>4</sub>Te Alloy

### 2.2.1 Introduction

In the previous chapter, the incorporation of Ti in Sb<sub>2</sub>Te has been proved to improve the thermal stability, and retains the rapid switching characteristic. Considering the acceleration of crystallization rate by increasing Sb/Te ratio, Sb–Te alloy with higher Sb concentration is easier to satisfy the requirement of replacing DRAM [28]. Thus, here, with the hope of getting faster operation rate, Ti is added in Sb<sub>4</sub>Te, which is still in  $\delta$  phase and has the lowest melting point [29].

There is another research priority in this work. In 2005, Kifune et al. inferred the structure of Sb–Te alloy through studying Sb<sub>72</sub>Te<sub>28</sub> and Sb<sub>85</sub>Te<sub>15</sub> by using synchrotron radiation XRD and SAED [24]. As seen in Fig. 2.6, the stacking number is a function of Te concentration. In 2014, they revised their models [30]. The chemical formula of Sb–Te alloy in  $\delta$  phase can be described as (Sb<sub>2</sub>)<sub>n</sub>(Sb<sub>2</sub>Te<sub>3</sub>)<sub>m</sub>, where n and m are integers. The stacking rule is that, when the value of n/m is an integer, two Sb<sub>2</sub>Te<sub>3</sub> blocks are separated by the number of n/m Sb<sub>2</sub> blocks. Take Sb<sub>4</sub>Te as an example, the chemical formula can be re-described to (Sb<sub>2</sub>)<sub>5</sub>(Sb<sub>2</sub>Te<sub>3</sub>), in which n/m = 5. Thus, the stacking structure is



when the value of n/m is not an integer, then these Sb<sub>2</sub>Te<sub>3</sub> blocks would be separated by the two integers close to n/m. For example, the chemical formula of



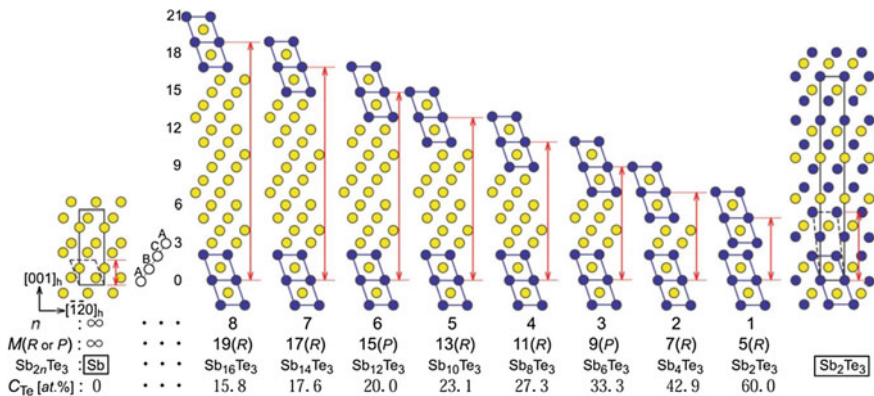
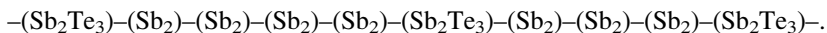


**Fig. 2.6** Kifune et al. infer the crystal structure of Sb–Te alloy, in which the stacking number is a function of Te concentration [24]

Sb<sub>3</sub>Te also can be re-described to (Sb<sub>2</sub>)<sub>7</sub>(Sb<sub>2</sub>Te<sub>3</sub>)<sub>2</sub>, in which  $n/m = 3.5$ . The above and below integers are 4 and 3, respectively. So, the stacking structure becomes



Before these studies, the crystal structure of Sb–Te alloy is not clear except for Sb<sub>2</sub>Te<sub>3</sub> and Sb<sub>2</sub>Te. So this finding is very helpful to understand Sb–Te alloy on an atomic scale. However, there is still little further work confirming the interesting stacking rule. Therefore, in this work, the influence of Ti on the thermal stability and crystallization speed of Sb<sub>4</sub>Te will be investigated. Also, the crystal structure of Sb<sub>4</sub>Te before and after Ti doping will be discussed.

## 2.2.2 Experimental Section

The Sb<sub>4</sub>Te and Ti-doped Sb<sub>4</sub>Te alloys were deposited on a SiO<sub>2</sub>/Si (100) substrate using Sb, Te, and Ti targets. Sheet resistance versus temperature was studied by Linkam LMP 95 hot stage. Differential scanning calorimetry (DSC) was used to analyze the crystallization temperature and melting temperature of TST powder. The powder sample was prepared by the following procedure. Film of 1 μm thickness was deposited on Si substrate which was covered by thick photoresist. Thin film was separated from the substrate by dissolving the photoresist with acetone. The residue was finally used for DSC measurement after drying. T-shaped test cells with 190 nm-diameter tungsten-heating electrodes have been fabricated using 0.13 μm CMOS technology. Then ~150 nm TST film was deposited above the heating electrode, followed by TiN adhesion layer and Al top electrode. The electrical properties of TST-based PCM were measured by a Keithley 2400C and a Tektronix AWG5002B pulse generator. Besides, ~20 nm thickness ST and TST



films were directly deposited on ultra-thin carbon film, and were studied by FEI Tecnai F20 transmission electron microscope (TEM) in bright, high-resolution TEM (HRTEM) as well as in SAED mode. In addition, the compositions of 100-thickness ST and TST films, which were deposited on aluminum foil, were determined by energy dispersion X-ray spectrometry (EDX; Oxford INCA Energy equipped in Hitachi S4700 scanning electron microscope).

2.2.3 Thermal Stability

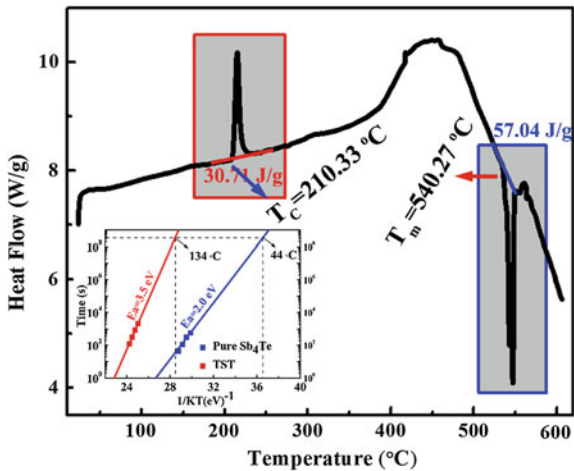
Compositions of ST and TST films are shown in Table 2.1, which are repeatedly measured. For ST film, the Sb/Te is very close to 4/1. However, in the case of TST film, Te concentration is almost unchanged when Sb content decreases sharply. Remarkably, the atomic ratio (Ti + Sb)/Te  $\approx$  4/1, and has the chemical formula of Ti<sub>x</sub>Sb<sub>80-x</sub>Te<sub>20</sub> (x  $\approx$  10). The phenomenon is often observed in substitution alloys [31, 32].

To measure the  $T_C$  and  $T_m$  of TST, DSC was carried out, the results of which are shown in Fig. 2.7. The heating speed was also set to 10 °C/min. From the DCS curve, we can find one sharp exothermic peak along 210.33 °C, which corresponds

**Table 2.1** Analyzed composition of sputtered Sb<sub>4</sub>Te and Ti-doped Sb<sub>4</sub>Te films

Composition	Ti (at. %)	Sb (at. %)	Te (at. %)	Total (at. %)
Sb <sub>4</sub> Te-1	–	79.94	20.06	100
Sb <sub>4</sub> Te-2	–	79.30	20.70	100
Sb <sub>4</sub> Te-3	–	79.94	20.06	100
TST-1	9.24	71.06	19.70	100
TST-2	9.34	71.67	18.99	100
TST-3	10.22	70.35	19.42	100

**Fig. 2.7** The DSC curve of TST powder. The inset shows the data retention of ST and TST films. TST film has a crystallization temperature of 210.33 °C and melting point of 540.27 °C



to  $T_C$ . This is because that the crystalline state is more stable than the amorphous state, and has lower internal energy. The  $T_C$  of ST is much higher than ST ( $\sim 132$  °C [33]) and GST ( $\sim 150$  °C) films, which will make the amorphous state more stable. Besides, a prominent endothermic peak appears at 540.27 °C, which indicates that TST begins to melt. After Ti doping, although no big change, the  $T_m$  further drops. The  $T_m$  of TST is almost 80 °C lower than that of GST [33]. A higher  $T_C$  is very helpful for realizing data storage. In addition, much lower  $T_m$  can reduce the damage on phase-change material during the Reset operation, and thereby prolongs PCM cell life. Confusingly, the baseline of the DSC curve almost lineally ascends with increasing temperature while a wide exothermic phenomenon is also observed along 400 °C. The mismatch of the thermal capacities of TST and Al crucible is responsible for the phenomenon. The only crystallization and melting peaks in the DSC curve demonstrates that TST has one phase transition process and is an equilibrium phase. This further supports the possibility of Ti substitution of Sb in TST alloy.

The data retention characteristics of ST and TST can be estimated by failure-time at various isothermal annealing temperatures, as shown in the inset of Fig. 2.7. The 10-year lifetime for ST is only 44 °C, which indicates that ST is not suitable for application in PCM without doping. The activation energy ( $E_a$ ) of 2.0 eV also implies that just a low energy will lead to the spontaneous crystallization of the amorphous ST film. However, the 10-year data retention temperature for TST is improved to 134 °C, 90 °C higher than that of ST. The result is also much better than that of GST (85 °C) 3.5 eV  $E_a$  makes the amorphous TST difficult to spontaneous crystallization.

### 2.2.4 Crystalline Structure

Above studies have proved that, consisting with our assumption, the thermal stability of ST is significantly enhanced by doping Ti, and the  $T_m$  is still low. Next, the structure of ST and TST is characterized by TEM. In order to get crystalline ST and TST, both films were annealed at 250 °C for 2 min. From Fig. 2.8a, we can find that ST film has completely crystallized and is divided into several pieces. The grain size is larger than 1  $\mu\text{m}$ , which will lead to poor adhesion with the substrate in PCM fabrication process and the easy formation of cavity. Through the enlarged Fig. 2.8b, clear grain boundaries are observed in the sample. Owing to the overgrowth of grains, neighboring grains squeeze each other, which results in the fluctuant surface.

The HRTEM image in Fig. 2.8c displays the regular atomic arrangement along the same crystal orientation. By the measurement of 32 crystal lattices, as exhibited in Fig. 2.8e, the average interplanar spacing is calculated to be 3.088 Å. The electron diffraction pattern in Fig. 2.8d presents diffraction spots with two periodically arranged (marked by OC and AB). This indicates that there are two structures periodically stacked in the unit cell of the ST alloys, which is often observed in Sb-rich Sb–Te binary [34, 35]. Previous studies show that  $\delta$  phase Sb–Te alloys present an A7-type structure of Sb and can be described by a

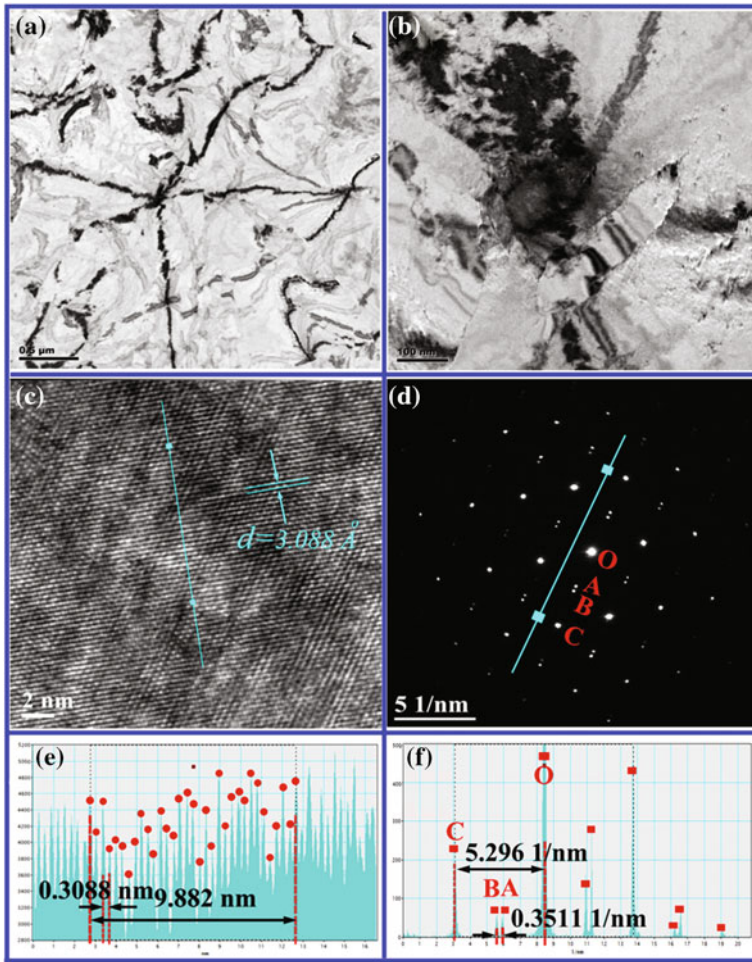


**Fig. 2.8** **a–b** TEM images with different resolutions, **c** HRTEM image and **d** SAED pattern for crystalline ST sample. The corresponding intensity line profiles of **a** HRTEM image and **d** SAED pattern, respectively

two-sublattice model [29]. One sublattice with three sites per formula unit is stacked by alternate Sb and Te atoms. The other one with two sites per formula unit is occupied only by continuous Sb atoms. Thus, in the reciprocal space, the distance between the nearest reciprocal lattice points A and B represents the length of the unit cell while that of OC corresponds to the interplanar space of one atomic layer along  $c$  axis. From the ratio  $M$  between OC and AB, we can infer the number of atomic layers of a unit cell. As shown in Fig. 2.8f, the value of OC is 5.2961 1/nm, which is 15 times than that of AB (0.3511 1/nm). Thus, the stacking period of ST is 15 layers.

According to Kifune et al. research, the stacking period ( $M$ ) can be expressed by formula:  $M = 3 \times 100/C_{Te}$ , where  $C_{Te}$  is Te atomic percent in Sb-Te alloy [24]. Since the  $C_{Te}$  of ST alloy is 20%, the theoretical value of  $M$  is 15, which agrees well with the experimental result. Therefore, the structure of ST alloy consists of 15 layers stacked along the  $c$  axis and is the combination of 5 layers stacks of  $Sb_2Te_3$  and 10 layers stacks of Sb. The stacking sequence is—Te-Sb-Te-Sb-Sb-Sb-Sb-Sb-Sb-Sb-Sb-Sb-Sb-Te-Sb—.

After doping Ti, the morphology undergoes great changes, as shown in Fig. 2.9a and b. The most obvious difference is that, compared to large grains with a bumpy surface of ST film, TST film is covered by alternating white and dark domain with much smaller size, and the surface is smoother. The grain size for TST films is just

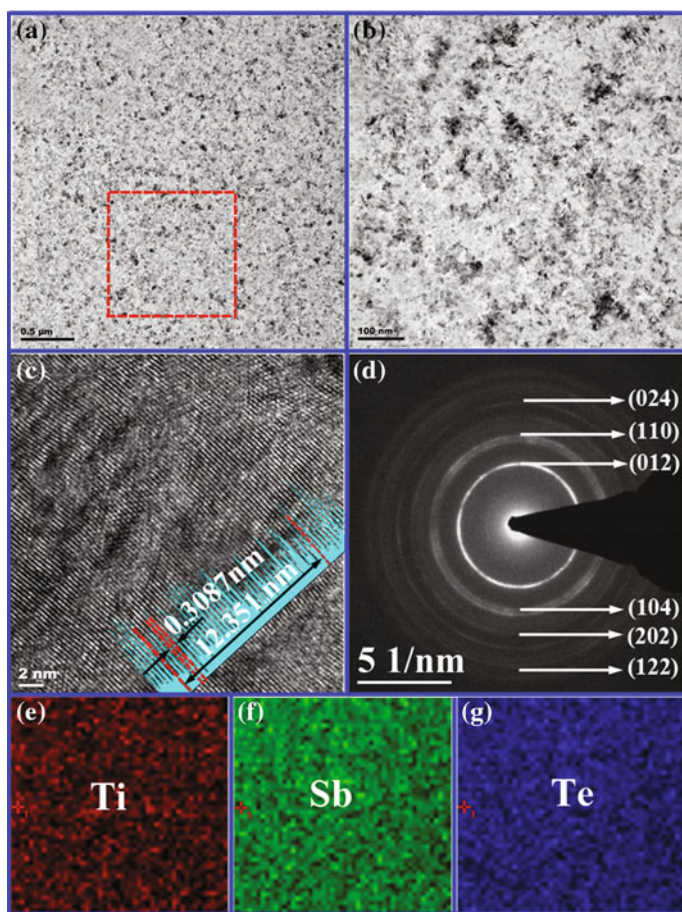


**Fig. 2.9** a–b TEM images with different resolutions, c HRTEM image and d SAED pattern for crystalline TST sample. e–g The element mapping of Ti, Sb, and Te in TST film. The area is marked by dotted box in figure a

dozens of nanometers, which will improve the adhesion with the substrate in PCM fabrication process and accelerate the crystallization process [36]. From the HRTEM image (Fig. 2.9c), it can be seen that many defects and lattice disorders take place due to Ti doping. In addition, interplanar spacing is 3.087 Å, a little smaller than that ST film. It has been reported that the substitution of Ti atom for Sb atom, owing to its smaller covalent radii, can lead to the decrease in lattice parameters and unit cell volume. This is probably the reason for the decreasing interplanar spacing and lattice disorder in TST. The concentric rings in the SAED pattern, as shown in Fig. 2.9d, indicate that TST is formed into polycrystalline phase. Through indexing, the crystalline TST can be assigned to rhombohedral structure of Sb, the same as ST. (102) crystal face is the preferential orientation plane, the lattice of which has shown in Fig. 2.9c. No other phase contains Ti is found in TST. Elemental mapping images of TST film, shown in Fig. 2.9e–g, demonstrates the presence of Ti, Sb, Te elements obtained by EDX in scanning TEM mode. The element color mapping of Ti in Fig. 2.9e reveals the uniform spatial distribution of Ti element in TST film. Furthermore, no cluster and cavity of Sb and Te elements is observed in Fig. 2.9f and g, respectively. From above experimental results, the incorporation of Ti atoms into the ST crystal lattice can only be achieved by replacing Sb atoms.

### 2.2.5 Device Performance

For N, [37] Si doping, [38, 39] the impurities often exist in grains in the form of amorphous phase or by-products, which remarkably inhibits the crystallization process of phase-change materials. Nevertheless, substitutional Ti atoms in TST could significantly improve the thermal stability without severely affecting the crystallization process. The effect can be confirmed through measuring the device performance of TST-based PCM. The cross-section of T-shape PCM cell used in our experiments is presented in the inset of Fig. 2.10a. Figure 2.10a shows the typical resistance–voltage ( $R$ – $V$ ) curves for the PCM cell. Applying 200 ns pulses, the amorphous state cell can switch to highly conductive state (Set operation) at 0.9 V voltages. Then the resistance hardly changes with increasing voltage until 3.5 V, at which the applied energy is enough to melt the TST (Reset operation), and results in high resistance of the cell. The Set and Reset voltages are smaller than those of GST-based device (1.2 and 4 V, respectively) [40]. This is attributed to the much lower  $T_m$  of TST. The reduction of pulse length leads to a little increase in the Set and Reset voltages. Noticeably, TST-based cell can achieve reversible phase transition with only 20 ns pulse, which is much faster than GST-based one [41]. For investigating the crystallization rate in more detail, the required time for Set operation was measured as a function of pulse length with different amplitudes, as shown in Fig. 2.10b. The Set state test cell was re-derived to Reset state by employing high amplitude pulse each time. From the figure, we can see that, because of unsatisfied energy, no change takes place until giving 0.8 V voltages.



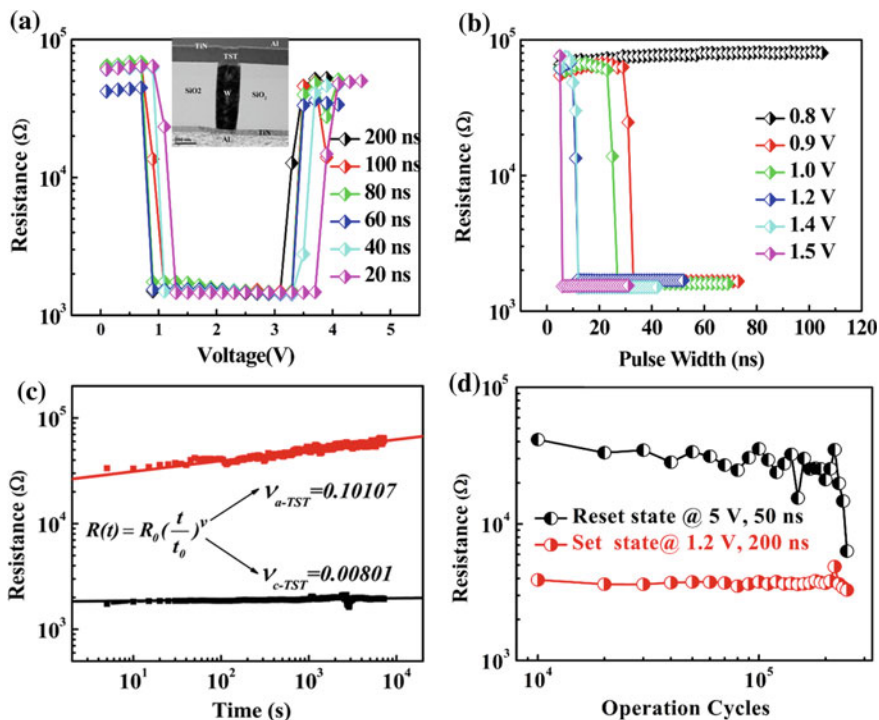


**Fig. 2.10** **a** Resistance–voltage curves of PCM based on TST film. The inset shows the cross-sectional structure of a PCM cell. **b** Set speed of TST-based PCM cell. **c** Measured resistance as a function of time for TST-based PCM cell in Set and Reset states. **d** Endurance characteristics of TST-based PCM cell

Just increase the pulse amplitude to 0.9 V, the cell can switch from high resistance state to a highly conductive state at 33 ns. Further increasing the voltage, smaller time is required to achieve Set operation. Remarkably, only 6 ns crystallization speed is obtained in TST-based PCM by 1.5 V voltages, which even can satisfy the rigors requirement of DRAM. According to the previous analysis, it can be concluding that the substitution of Ti for Sb and the reduction of grain are responsible for quick crystallization rate of TST.

An ideal nonvolatile memory would require both amorphous and crystalline phases to be thermodynamically stable without operations. However, not only the spontaneous crystallization, but also the resistances drift will affect the reliability of PCM. Thus, in there, the time-evolution of the resistances for TST-based PCM in both Reset and Set states at room temperature are reported in Fig. 2.10c. The resistances were measured immediately after Reset and Set operations. A voltage pulse with an amplitude of 0.1 V, much lower than threshold voltage, was applied to read the cell resistance. As exhibited in Fig. 2.10c, crystalline resistance is highly

stable with time, which shows a near zero slope. However, amorphous resistance steadily increases with time. It has been proved that the variation of amorphous resistance results from structural relaxation of amorphous chalcogenide [42–44]. Structural relaxation is a short-range atomic rearrangement, which is ubiquitously found in amorphous semiconductor and metallic glasses [45–47]. The resistance drifts can be represented by the power law,

$$R(t) = R_0 \left( \frac{t}{t_0} \right)^v,$$

where  $R_0$  is the related value of resistance,  $t_0$  is an arbitrary time we fixed at the end of the recovery time, and  $v$  is the drift coefficient. The drift coefficient for Reset state is 0.10107, which indicates that amorphous resistance spontaneously increases after amorphization. However, the fluctuation of amorphous resistance of TST-based device is smaller than that of GST-based device ( $v = 0.11$ ) [43]. The reduction of resistance drift will improve the reliability of PCM.

Finally, endurance is evaluated to identify the reliability of TST-based PCM cell, as shown in Fig. 2.10d. The applied pulse widths/amplitudes are set to 200 ns/1.2 V and 50 ns/5 V for Set and Reset operations, respectively. The reversible operations can maintain above 2E5 cycles with very stable Set resistance and a little fluctuation in Reset resistance.

### 2.2.6 Summary

In this work, data retention of Sb<sub>4</sub>Te is significantly improved to 134 °C@10-year after doing Ti, although the resistance ratio is sacrificed. DSC results show that 9.5 at. % Ti-doped Sb<sub>4</sub>Te (TST) has a very low melting temperature of 540.27 °C while 620 °C for GST, which means that TST has the potential of low energy consumption. Crystalline ST film exhibit large grain size, an A7-type structure of Sb, and consists of 15 layers stacked along the *c* axis, which is the combination of 5 Sb<sub>2</sub>Te<sub>3</sub> layers and 10 Sb layers. TST has been proved to have the same crystalline structure as ST while grain size is decreased to nanoscale and abundant lattice disorders are discovered. Combining the result of EDX, DSC, and TEM, it can be concluded that Ti atoms occupy the lattice sites of Sb atoms in TST. This combination method has little influence on crystallization speed, which has been proved by high device performance of TST-based PCM cell. 6 ns crystallization rate is obtained in TST-based device, more than 10 times faster than that of GST-based one. Set and Reset voltages are also lower, which demonstrate that less energy consumption is required to operate the TST-based device. This is attributed to the low melting point of TST. The resistance drift phenomenon is also observed in TST-based cell, however, the drift coefficient is smaller than GST, which benefits for the reliability of PCM.



## 2.3 Ti-Doped Sb<sub>2</sub>Te<sub>3</sub> Alloy

### 2.3.1 Introduction

In our previous work, Ti was doped in Sb<sub>2</sub>Te and Sb<sub>4</sub>Te alloy for getting rapid crystallization speed and good data retention [48, 49]. Unfortunately, the resistance ratio between high and low sheet resistances was sharply decreased, which seriously reduces the sensing margin of PCM.

In this work, we find that the incorporation of Ti in Sb<sub>2</sub>Te<sub>3</sub> not only can improve the thermal stability, but also increase the sheet resistance ratio. In order to find the reasons for this phenomenon, the carrier concentration and mobility, which are the decisive factors of sheet resistance, are measured by Hall system. Besides, the effects of Ti doping on the structure and phase-change characteristics of Sb<sub>2</sub>Te<sub>3</sub> are also investigated in detail.

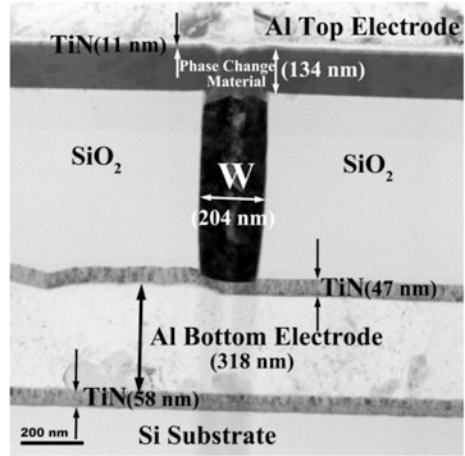
### 2.3.2 Experimental Section

The Ti-doped Sb<sub>2</sub>Te<sub>3</sub> (TST) films with different thicknesses were deposited by the cosputtering of Ti and Sb<sub>2</sub>Te<sub>3</sub> targets on SiO<sub>2</sub>/Si substrates using a RF sputtering system at room temperature. Sb<sub>2</sub>Te<sub>3</sub> films were also prepared for comparison. The carrier density and mobility were determined using homemade Hall system with a Keithley 2000 and a Keithley 2400 in the magnetic field intensity of 0.5T. For real-time observation of the structure transition for pure Sb<sub>2</sub>Te<sub>3</sub> and TST films (200 nm), the in situ XRD was performed using PANalytical X'Pert PRO diffraction with Cu K $\alpha$  ( $\lambda = 0.15418$  nm) radiation source. 20 nm-thick Sb<sub>2</sub>Te<sub>3</sub> and TST films were directly deposited on supporting grids coated with carbon film, and annealed at 250 °C for 2 min. Then these samples were studied by FEI Tecnai F20 TEM in bright field, HTEM as well as in selected area diffraction (SAED) mode. Nova 200 Nanolab Focused ion beam (FIB) was employed to prepare the cross-sectional structure of the PCM cell, which was observed by TEM, as shown in Fig. 2.11. The resistance–voltage and programming cycle tests were performed by a Keithley 2400C and a Tektronix AWG5002B pulse generator.

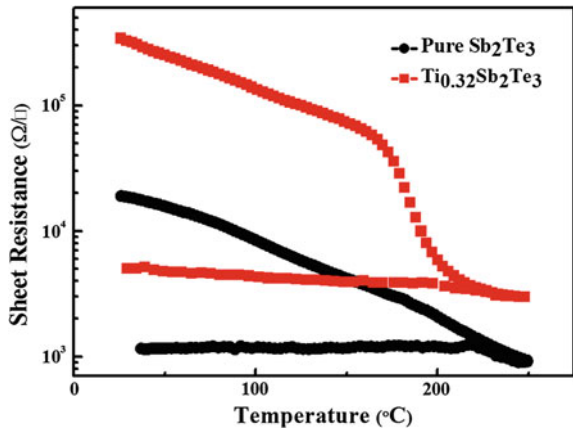
### 2.3.3 Thermal Stability

Figure 2.12 shows the sheet resistance–temperature ( $R$ – $T$ ) curves of pure Sb<sub>2</sub>Te<sub>3</sub> and TST films. As shown in this figure, a slow and gradual drop of sheet resistance is observed for pure Sb<sub>2</sub>Te<sub>3</sub>. This is because that as-deposited Sb<sub>2</sub>Te<sub>3</sub> film has partial crystallization due to its low crystallization temperature (<100 °C), which will be confirmed by subsequent XRD experiments. Unlike the  $R$ – $T$  curve for pure

**Fig. 2.11** Cross-sectional TEM image of TST-based PCM cell. The cell is fabricated by a 0.13  $\mu\text{m}$ -node CMOS technology



**Fig. 2.12** Sheet resistances versus temperature measurements for as-deposited  $\text{Sb}_2\text{Te}_3$  and TST films. The heating rate is 10  $^{\circ}\text{C}/\text{min}$ . The initial resistance for as-deposited  $\text{Sb}_2\text{Te}_3$  is very low because of partial crystallization. The resistance ratio is much increased after Ti doping



$\text{Sb}_2\text{Te}_3$ , a sudden resistance drop, corresponding to crystallization temperature ( $T_C$ ), happens at 175.6  $^{\circ}\text{C}$  for TST sample. The value is much higher than that of pure  $\text{Sb}_2\text{Te}_3$  and conventional GST films ( $\sim 150$   $^{\circ}\text{C}$ ). The high  $T_C$  will make the amorphous state more stable. It is worth to point out that the resistance contrast between initial and crystalline states for TST film is also remarkably increased. A large resistance contrast will provide a large sensing margin for PCM applications. Simultaneously, the crystalline  $R$  increases to  $3 \times 10^3$   $\Omega/\text{Sq}$ , benefiting for reducing the Reset current in PCM [50]. Since Ti is a metal, the decreases of crystalline and amorphous  $R$  after doping Ti are easy to understand, which were observed in Ti-doped  $\text{Sb}_2\text{Te}$  alloy reported before [48]. However, the  $R$  variations of Ti-doped  $\text{Sb}_2\text{Te}_3$  are much different.

In order to find the reasons, the carrier concentration and mobility, which are the determining factors of  $R$ , were measured by Hall system at room temperature. The values of these parameters are summarized in Table 2.2. It is necessary to point out

**Table 2.2** Results of Hall effect measurements for pure Sb<sub>2</sub>Te<sub>3</sub> and TST films

Sample	Amorphous				Crystalline			Type
	Carrier density cm <sup>-3</sup>	Mobility cm <sup>2</sup> V <sup>-1</sup> s <sup>-1</sup>	Hall coefficient cm <sup>3</sup> C <sup>-1</sup>		Carrier density cm <sup>-3</sup>	Mobility cm <sup>2</sup> V <sup>-1</sup> s <sup>-1</sup>	Hall coefficient cm <sup>3</sup> C <sup>-1</sup>	
Sb <sub>2</sub> Te <sub>3</sub>	7.93 × 10 <sup>19</sup>	3.96	0.0597		1.42 × 10 <sup>20</sup>	31.8	0.0431	<i>P</i>
Ti <sub>0.32</sub> Sb <sub>2</sub> Te <sub>3</sub>	2.32 × 10 <sup>20</sup>	0.416	0.0270		1.50 × 10 <sup>21</sup>	0.551	0.00415	<i>P</i>

that both Sb<sub>2</sub>Te<sub>3</sub> and TST films are p-type semiconductor. The antisite defect, the excess of Sb replacing the Te lattices, is responsible for the carrier type of Sb<sub>2</sub>Te<sub>3</sub> [51]. The reason for *p*-type TST films will be carefully discussed elsewhere. A carrier concentration of  $7.93 \times 10^{19} \text{ cm}^{-3}$  is found for as-deposited Sb<sub>2</sub>Te<sub>3</sub> (A-Sb<sub>2</sub>Te<sub>3</sub>), which agrees well with other reports [52]. Apparently, the carrier density for as-deposited TST (A-TST) film slightly increases to  $2.32 \times 10^{20} \text{ cm}^{-3}$  while the mobility ( $\mu_p$ ) sharply drops to only  $0.416 \text{ cm}^2\text{V}^{-1}\text{s}^{-1}$ , just one-tenth of that for A-Sb<sub>2</sub>Te<sub>3</sub> film. According to the equations of  $R = \rho/d$  and  $\rho = 1/pq\mu_p$ , where  $\rho$  is the resistivity,  $p$  is the hole concentration and  $q$  is the electric charge, the rapid reduction in mobility for TST will increase the initial  $R$ , as exhibited in the  $R$ - $T$  curve. After 250 °C-annealed, the mobility for crystalline Sb<sub>2</sub>Te<sub>3</sub> (C-Sb<sub>2</sub>Te<sub>3</sub>) film rises up to  $31.8 \text{ cm}^2\text{V}^{-1}\text{s}^{-1}$  with a small increase in carrier concentration. The augment in mobility for C-Sb<sub>2</sub>Te<sub>3</sub> film is mainly due to weak lattice scattering for the more regular atomic arrangement. In contrast, crystalline TST (C-TST) film shows a higher carrier density of  $1.5 \times 10^{21}$ , however, the mobility is still very low ( $0.551 \text{ cm}^2\text{V}^{-1}\text{s}^{-1}$ ). Therefore, the decrease in mobility is also the main factor for the increasing crystalline  $R$  of TST film. From the low mobility of TST film, no matter amorphous or crystalline state, it can be concluded that the impurity scattering, replacing the lattice scattering, becomes the dominating factor that affects the mobility of TST alloy, which ultimately results in the different  $R$  changes.

### 2.3.4 Crystalline Structure

Figure 2.13 shows the in situ XRD patterns of pure Sb<sub>2</sub>Te<sub>3</sub> and TST films. Some diffraction peaks appear in the as-deposited Sb<sub>2</sub>Te<sub>3</sub> film, which indicate that it has crystallized during the sputtering process. The diffraction peaks in 29.67° and 42.30° correspond to (200) and (220) crystal faces of face-centered cubic (FCC) structure, respectively. The phase transition from the FCC to hexagonal

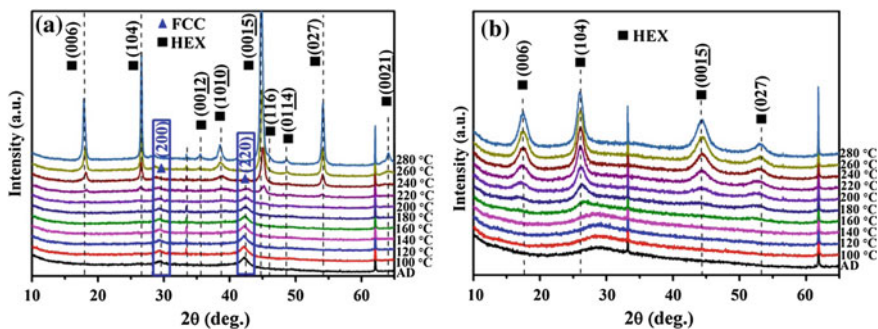


**Fig. 2.13** In situ XRD results for pure Sb<sub>2</sub>Te<sub>3</sub> (a) and TST (b) films, respectively. The Sb<sub>2</sub>Te<sub>3</sub> film shows a metastable phase of FCC structure while only HEX phase is found in crystalline TST film

(HEX) structure takes place at 220 °C, coinciding with the results of Yin et al. [53]. In contrast to pure  $\text{Sb}_2\text{Te}_3$  film, the as-deposited TST film is amorphous. With the increase of annealing temperature, amorphous TST film crystallizes gradually and HEX is the only crystalline structure. Observably, the  $T_C$  for TST film is between 160 and 180 °C, which is consistent with the result of  $R$ – $T$  curve. It is notable that besides the  $\text{Sb}_2\text{Te}_3$  phase, no other crystalline structure forms in TST. Phase separation, frequently caused by doping, severely limits the crystallization speed and deteriorates device performance [54]. Therefore the uniform structure is very benefit for the operation speed and reliability of TST-based PCM.

The morphologies of crystalline  $\text{Sb}_2\text{Te}_3$  and TST films were characterized by TEM, HRTEM, and SAED, as shown in Fig. 2.14a–d and e–h, respectively. From Fig. 2.14a, we can see that crystalline  $\text{Sb}_2\text{Te}_3$  film consists of irregular shape grains. The grain size reaches several hundred nanometers. The grain boundaries between light and dark grains are observed clearly, as shown in Fig. 2.14b. Analyzing the HRTEM image of the centric grain in Fig. 2.14b, as seen in Fig. 2.14c, two lattice fringes with the same spacing of 2.13 Å form an included angle of 60°, corresponding to the {110} planes of HEX phase  $\text{Sb}_2\text{Te}_3$ . The deduction can be confirmed by the SAED pattern in Fig. 2.14d. Compared to pure  $\text{Sb}_2\text{Te}_3$ , as shown in Fig. 2.14e, the grain size of TST film is much smaller ( $\sim 50$  nm). Through detailed observation (Fig. 2.14f), the film is completely crystallized with polygonal grains of homogeneous size, and no amorphous material exists in the grain boundary. The HRTEM of the TST in Fig. 2.14g displays a similar atomic arrangement of pure  $\text{Sb}_2\text{Te}_3$  film. The SAED pattern in Fig. 2.14h exhibits polycrystalline rings with scattered diffraction spots. Through indexing, the TST film can be assigned to HEX  $\text{Sb}_2\text{Te}_3$  structure. No other diffraction ring belonging to Ti, TiSb, TiTe phases is found, consistent with the XRD results.

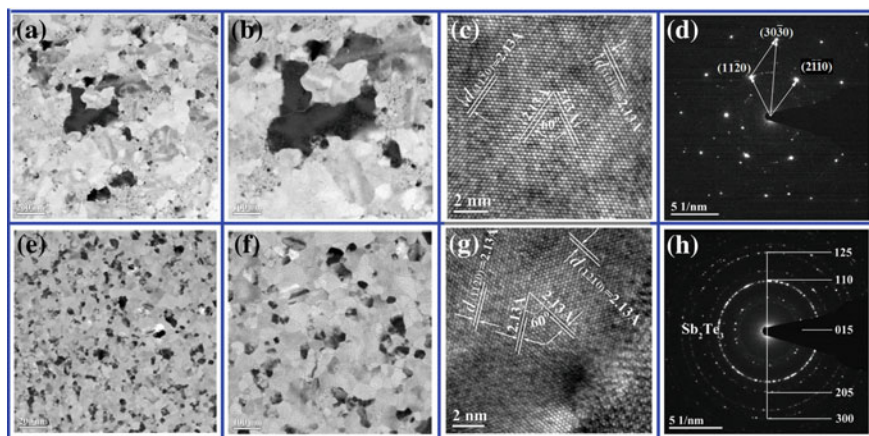


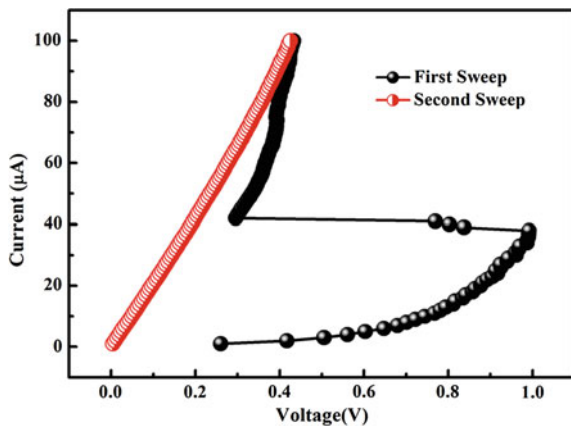
**Fig. 2.14** a–b TEM images with different resolutions, c HRTEM image and d SAED pattern for pure  $\text{Sb}_2\text{Te}_3$  sample. e–f TEM images with different resolutions, g HRTEM image and h SAED pattern for TST sample

Based on the XRD and TEM results, the obvious distinction between crystalline  $\text{Sb}_2\text{Te}_3$  and TST film is the grain size. For other doping, such as N, [53]  $\text{SiO}_2$ , [55] Si, [56]-doping, the striking reduction of grain size is because that amorphous dopants or by-products exist in the grain boundary, which remarkably inhibit the crystalline process. Meanwhile, the inhibiting effect will result in the slow of the crystalline rate [57]. However, as shown in the TEM image in Fig. 2.14f, there is nothing in the grain boundary of TST film, different from other doping. The reasons for the reduction of the grain size can be explained as followed: The crystalline process of phase-change material mainly involves crystal nucleation and crystal growth. Besides, it typically starts at defects in the film and interfaces [53]. In the case of TST film, a small amount Ti in the  $\text{Sb}_2\text{Te}_3$  destroys the crystal perfection and the point defects will be significantly increased. As the crystal nucleation usually starts at defects, more point defects mean more nucleation centers. In the same volume, the grain size should be decreased to maintain the balance. It should be emphasized that the reduction of the grain size will accelerate the crystalline rate [58]. This is because that smaller grain sizes have a larger fraction of interface areas. They can generate a higher concentration of free electrons and induce a more pronounced displacement of ions, resulting in a rapid change in the atomic structures [59].

### 2.3.5 Device Performance

Next, the PCM devices employing TST films were fabricated. GST-based PCM devices were also prepared for comparison. Figure 2.15 presents the current–voltage ( $I$ – $V$ ) curves for TST-based PCM cells. Initially, for the high resistance of the amorphous state, the voltage increases sharply with applied current. The low conductive state is maintained until the threshold voltage  $V_{\text{th}} = 1.0$  V is reached, with threshold current  $I_{\text{th}}$  of 38  $\mu\text{A}$ . After switching, the voltage drops suddenly and the device transforms into a highly conductive state.

**Fig. 2.15** Current–voltage ( $I$ – $V$ ) curves for TST-based PCM cells. During the first sweep, the device exhibits threshold switching phenomenon, and the threshold voltage is 1.0 V



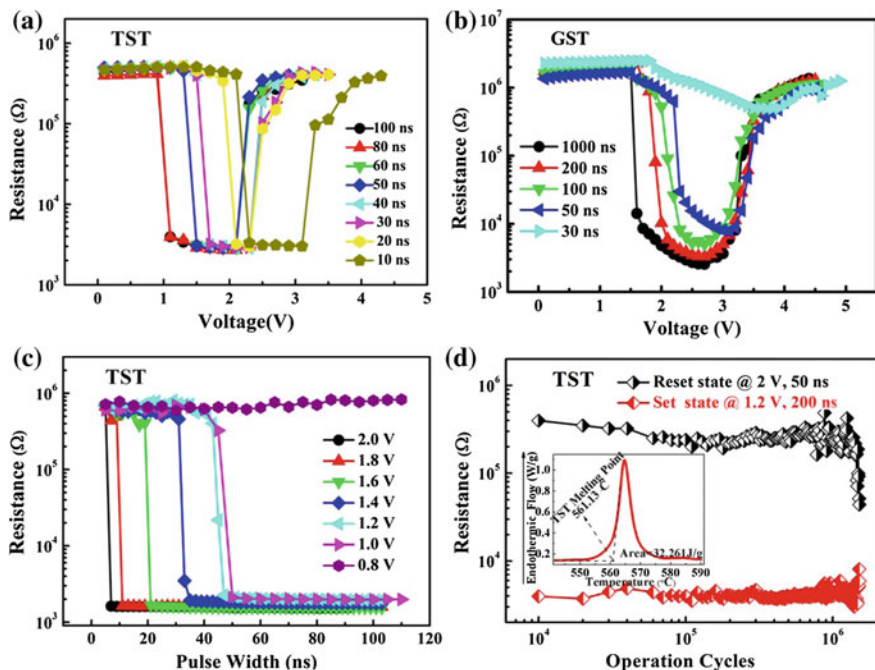


**Fig. 2.16** Cell resistances measured as a function of the voltage pulse with different pulse lengths for **a** TST and **b** GST-based PCM cells. **c** The Set speed for TST-based PCM cell. The inset shows the cross-sectional structure of a PCM cell. **d** Endurance characteristics of TST-based PCM cell. The inset shows the DSC curve of TST powder with heating rate of 10 °C/min

Figure 2.16a–b shows the resistance–voltage ( $R$ – $V$ ) characteristics of the PCM cells with TST and GST films, respectively. At the pulse length of 100 ns, the Set operation for TST test cell is achieved by the pulse amplitude of 1.1 V, which is just half of that for GST-based PCM cell (2.3 V). The high Set voltage for GST-based device even can satisfy the requirement of a Reset operation for TST-based device. The Reset operation voltage is also much lower than that of Ti-doped  $\text{Sb}_2\text{Te}$  based cell ( $\sim 3.6$  V@100 ns) [48]. In addition, for TST-based device, except for the Set and Reset operation, the resistances almost do not change with increasing pulse amplitude. Noticeably, the cell can readily achieve complete Set and Reset operation using 10 ns pulse. This proves that TST test cell has the capability of high-speed operation.

By contrast, as shown in Fig. 2.16b, the resistances of conventional GST-based PCM cells are more sensitive to the pulse voltage and pulse width. Obviously, below 100 ns, the Set operation for GST PCM cells is incomplete with abnormal Set resistance while already cannot be achieved by 30 ns pulse. Therefore, compared with GST-based PCM cells, PCM devices based on TST films show a faster phase transition speed and more steady resistances. Besides, energy consumption of PCM cell is almost determined by the switching energy of Reset operation. The



switching energy for Reset operation can be estimated by  $E_{\text{Reset}} = \frac{U_{\text{Reset}}^2}{R_{\text{Set}}} t$  where  $R_{\text{Set}}$  is the Set resistance,  $t$  is the pulse width (100 ns), and  $U_{\text{Reset}}$  is the Reset voltage. Set resistance and Reset voltage for TST-based PCM cell are 2929  $\Omega$  and 2.3 V, respectively. Thus, the  $E_{\text{Reset}}$  for TST-based one is about  $1.80 \times 10^{-10}$  J. The Set resistance of GST-based PCM is very close to that of TST-based one (2572  $\Omega$ ), however, the Reset voltage is much higher (3.5 V). Therefore, the  $E_{\text{Reset}}$  for GST-based one increases to  $4.76 \times 10^{-10}$  J. Since the Reset operation needs to melt the phase-change material, the much lower melting point of TST alloy (561.13 °C) which is shown in the inset of Fig. 2.16d, compared to that of GST material ( $\sim 620$  °C), is responsible for the lower operation voltages and switching energy.

As one of the most critical parameters in PCM, the Set operation speed needs to be more detailed studied. Thus, the required time for Set ( $t_{\text{Set}}$ ) operation was individually measured as a function of applied pulse widths with different amplitudes, as shown in Fig. 2.16c. The  $t_{\text{Set}}$  for all PCM cells varies regularly with increasing pulse amplitude. Initially, the Set operation cannot be achieved (over hundreds of nanosecond) by employing pulse amplitude of 0.8 V. By applying 1.0 V voltage, the first switch to low resistance happens with  $t_{\text{Set}}$  of 50 ns. Further increasing the voltage, less  $t_{\text{Set}}$  is needed. Remarkably, the  $t_{\text{Set}}$  decreases to only 6 ns as the voltage larger than 2.0 V. The small grain size is one of the reasons for such extremely high speed of TST-based PCM. The operation speed of PCM using TST film is much faster than that of Flash ( $\mu\text{s}$ ), and even can satisfy the high demand of access times ( $\sim 10$  ns) for DRAM [60].

Figure 2.16d presents the endurance for TST-based PCM cells. Repeated Set and Reset operations are maintained more than  $1 \times 10^6$  cycles, better than that of Ti-doped Sb<sub>2</sub>Te and Ti-based Sb<sub>4</sub>Te based devices [48, 61]. Before failure, the Reset and Set resistance during cyclic operation are stable with a fluctuation in only half order of magnitude. Two feasible reasons are explained as follows: The first point, as mentioned above, is that the resistances of TST-based PCM cells are less sensitive to the pulse amplitude. The second point is that only one phase transition happens in TST film from the amorphous phase to the crystalline phase.

### 2.3.6 Summary

In summary, Ti-doped Sb<sub>2</sub>Te<sub>3</sub> alloy (TST) is proposed and investigated for PCM application. The crystallization temperature and the resistance contrast between amorphous and crystalline state are significantly increased. The impurity scattering in TST film leads to the great decrease in mobility, which ultimately results in the increase of amorphous and crystalline sheet resistance. The TST alloy has uniform crystalline phase with HEX structure and the grain size is distinctly decreased, which are important for improving device performance. The Set and Reset operation, for TST-based PCM, can be easily achieved by 10 ns pulse, much faster than

that of GST-based one. A Set operation speed of only 6 ns is exhibited, and a cyclic operation up to  $1 \times 10^6$  is obtained with a stable Reset and Set resistances. Such experimental results demonstrate that TST has great potential for high-speed PCM application, which will be systematical studied in the next chapter.

## 2.4 Conclusion

In this chapter, the influences of Ti doping on the thermal stabilities, crystalline structures and device performances of Sb–Te alloys are investigated:

1. After adding  $\sim 10$  at. % Ti, the crystallizations temperature of  $\text{Sb}_2\text{Te}$  and  $\text{Sb}_4\text{Te}$  increase to  $\sim 210$  °C, and the 10-year data retention temperature is  $\sim 130$  °C. For pure  $\text{Sb}_2\text{Te}$  and  $\text{Sb}_4\text{Te}$  alloys, the grain size is in the order of  $\mu\text{m}$ . With Ti doping, the grain size sharply reduces to the order of nm, which would enhance the adhesion with the substrate and accelerate the crystallization rate. The devices based on these alloys exhibit some advances, such as fast operation speed and low power consumption. Possessing endurances above  $10^5$ , PCM using these alloys has the potential to replace Flash memory.
2. By investigating the crystal structure of  $\text{Sb}_4\text{Te}$ , the atomic stacking rule of crystalline Sb–Te alloy, proposed by Kifune et al., is confirmed. The stacking number is a function of Te concentration.
3. Although the incorporation of Ti in Sb-rich Sb–Te alloy significantly improves thermal stability, the resistance ratio between high and low sheet resistances is decreased, which reduces the sensing margin of PCM. However, the incorporation of Ti in  $\text{Sb}_2\text{Te}_3$  not only can improve the data retention, but also raise the resistance ratio. The impurity scattering, which dramatically reduce the mobility, is responsible for the phenomenon.
4. PCM cells using Ti-doped  $\text{Sb}_2\text{Te}_3$  film demonstrate 6 ns crystallization speed and much lower required power compared to GST-based ones. Besides, endurances above  $10^6$  are achieved with stable high and low resistances.
5. Ti-doped  $\text{Sb}_2\text{Te}_3$  show a different grain refinement mechanism. The doped Ti would replace parts of Sb in the lattice, destroy the crystal perfection and increase point defects. Since the crystallization process of phase-change materials starts at defects, more defects mean more formed nuclei. In the same volume, the grain size should be reduced to keep the balance.

## References

1. S. Lai, T. Lowrey, in *IEDM Tech. Digest*, (2001), pp. 36.5.1–36.5.4
2. M. Wutting, *Nature Mater.* **4**, 265 (2005)
3. D. Loke, T.H. Lee, W.J. Wang, L.P. Shi, R. Zhao, Y.C. Yeo, T.C. Chong, S.R. Elliott, *Science* **336**, 1566 (2012)

4. G.W. Burr et al., J. Vac. Sci. Technol. **28**(2), 223 (2010)
5. I. Fridrich, V. Weidenhof, W. Njoroge, P. Franz, M. Wutting, J. Appl. Phys. **87**, 4130 (2000)
6. L. Rerniola et al., IEEE Electr. Device Lett. **31**, 488 (2010)
7. T.H. Jeong, M.R. Kim, H. Seo, J.W. Park, C. Yeon, Jpn. J. Appl. Phys. **39**, 2775 (2000)
8. B. Liu, T. Zhang, J.L. Xia, Z.T. Song, S.L. Feng, B. Chen, Semicond. Sci. Technol. **19**, L61 (2004)
9. K.B. Borisenko, Y.C.D.J.H. Cochayne, S.A. Song, H.S. Jeong, Acta Mater. **59**, 4335 (2011)
10. P. Noe, et al., in *IEDM*, (2012), p. 18.7.1
11. T.Y. Lee, S.S. Yim, D. Lee, M.H. Lee, D.H. Ahn, K.B. Kim, Appl. Phys. Lett. **89**, 163503 (2006)
12. W. Czubytyj, S.J. Hudgens, C. Dennison, C. Schell, T. Lowrey, I.E.E.E. Electr. Device Lett. **31**, 869 (2010)
13. C.M. Lee, et al., in *VLSI Technol.*, (2007), p. 12
14. W.D. Song, L.P. Shi, X.S. Miao, T.C. Chong, Appl. Phys. Lett. **90**, 091904 (2007)
15. K. Yusu, T. Nakai, S. Ashida, N. Ohmachi, N. Morishita, N. Nakamura, in *Proc. EPCOS*, (2005)
16. K. Wang, D. Wamwangi, S. Ziegler, C. Steimer, M. Wutting, J. Appl. Phys. **96**, 5557 (2004)
17. N. Yamada, E. Ohno, K. Nishiuchi, N. Akahira, M. Takao, J. Appl. Phys. **69**, 2849 (1991)
18. M.H.R. Lankhorst, L.V. Rieterson, M.V. Schijndel, B.A.J. Jacobs, J.C.N. Rijpers, Jpn. J. Appl. Phys. **4**, 863 (2003)
19. N. Kh. Abrikosov, L. V. Poretskaya, I. P. Ivanova, Zh. Neorg. Khim, **4**(11), 2525 (1959)
20. G. Ghosh, J. Phase Equilib. **15**, 349 (1994)
21. S. Fujimori, S. Yagi, H. Yamzaki, N. Funakoshi, J. Appl. Phys. **64**, 1000 (1988)
22. B.K. Cheong, S. Lee, J.H. Jeong, S. Park, S. Han, Z. Wu, D.H. Ahn, Phys. Status Solidi B **2012**, 10 (1985)
23. C. Drasar, M. Steinharta, P. Lost'ak, H. K. Shin, J.S. Dyck, C. Uher, *J. Solid State. Chem.* **178**, 1301 (2005)
24. K. Kifune, Y. Kubota, T. Matsunaga, N. Yamada, Acta Crystallogr. Section B **B61**, 492 (2005)
25. M. Zhu, L.W. Wu, F. Rao, Z.T. Song, X.L. Li, C. Peng, X.L. Zhou, K. Ren, D.N. Yao, S.L. Feng, J. Alloy Comp. **509**, 10105 (2011)
26. V.A. Kulbachinskii, N. Miura, H. Nakagawa, C. Drashar, P. Lostak, J. Phys. C: Solid State Phys. **11**, 5273 (1999)
27. S.M. Yoon, S.Y. Lee, S.W. Jung, Y.S. Park, B.G. Yu, Solid-State Electron. **53**, 557 (2009)
28. M.H.R. Lankhorst, L.V. Rieterson, M.V. Schijndel, B.A.J. Jacobs, J.C.N. Rijpers, Jpn. J. Appl. Phys. **4**, 863 (2003)
29. R. M. Imamov, S. A. Semiletov, Sov. Phys. Crystallogr. **15**(5), 845 (1971)
30. K. Kifue, T. Fujita, T. Tachizawa, Y. Kubota, N. Yamada, T. Matsunaga, Cryst. Res. Technol. **48**(11), 1011–1021 (2013)
31. Y.J. Chien, Z. Zhou, G. Uher, J. Crystal, Growth **283**, 309 (2005)
32. K.F. Kao, H.Y. Cheng, C.A. Jong, C.J. Lan, T.S. Chin, IEEE Trans. Electron Devices **43**, 930 (2007)
33. V.I. Kosyakov, V.A. Shestakov, L.E. Shelimova, F.A. Kuznetsov, V.S. Zemskov, Inorg. Mater. **36**, 1196 (2000)
34. V. Agafonov, N. Rodier, R. Ceolin, R. Bellient, C. Bergman, J.P. Caspard, Acta Crystallogr. **47**, 114 (1991)
35. M.S. Youm, Y.T. Kim, Y.H. Kim, M.Y. Sung, Phys. Stat. Sol. (a) **205**, 1636 (2008)
36. W.J. Wang, D. Loke, L.P. Shi, R. Zhao, H.X. Yang, L.T. Law, L.T. Ng, K.G. Lim, Y.C. Yeo, T.C. Chong, A.L. Lacaita, Scientific Reports **N2**, 360 (2012)
37. Y. Yin, Y. Yin, H. Sone, S. Hosaka, J. Appl. Phys. **10**, 064503 (2007)
38. Y. Cheng, Z.T. Song, Y.F. Gu, S.N. Song, F. Rao, L.C. Wu, B. Liu, S.L. Feng, Appl. Phys. Lett. **253**, 6125 (2007)
39. J. Feng, Z. F. Zhang, Y. Zhang, B. C. Cai, J. Appl. Phys. **101**, 074502 (2007)
40. S. Maitrejean, et al., in *IEEE ITC/MAM*, (2010), p. 13

41. K.F. Kao, C.M. Lee, M.J. Chen, M.J. Tsai, T.S. Chin, *Adv. Mater.* **21**, 1695 (2009)
42. M. Boniardi, A. Redaelli, A. Pirovano, I. Tortorelli, D. Ielmini, F. Pellizzer, *J. Appl. Phys.* **105**, 084506 (2009)
43. M. Boniardi, D. Ielmini, *Appl. Phys. Lett.* **98**, 243506 (2011)
44. S.B. Kim, B. Lee, M. Asheghi, F. Hurkx, J.P. Reifenberg, K.E. Goodson, H.S.P. Wong, *I.E.E. Trans, Electron Devices* **58**, 584 (2011)
45. D. Ielmini, A.L. Lacaita, *Mater. Today* **14**, 600 (2011)
46. S. Braga, A. Cabrini, G. Torelli, *Appl. Phys. Lett.* **94**, 092112 (2009)
47. N.M.J. Conway, A. Ilie, J. Robertson, W.I. Milne, A. Tagliaferro, *Appl. Phys. Lett.* **73**, 2456 (1998)
48. M. Zhu, L.C. Wu, Z.T. Song, F. Rao, D. Cai, C. Peng, X.L. Zhou, K. Ren, S.N. Song, B. Liu, S.L. Feng, *Appl. Phys. Lett.* **100**, 122101 (2012)
49. M. Zhu, L. Wu, F. Rao, Z. Song, X. Ji, D. Yao, Y. Cheng, S. Lv, S. Song, B. Liu, Xu Ling, *J. Appl. Phys.* **114**, 124302 (2013)
50. S.J. Ahn, Y.J. Song, C.W. Jeong, J.M. Shin, Y. Fai, Y.N. Hwang, S.H. Lee, K.C. Ryoo, S.Y. Lee, J.H. Park, et al., in *IEEE Electron Devices Meeting*, (2004), pp. 907–910
51. G.R. Miller, Che-Yu. Li, *J. Phys. Chem. Solids* **26**, 173 (1965)
52. Z. Stry, J. Horak, M. Stordeur, M. Stolzer, *J. Phys. Chem. Solids* **49**, 9 (1988)
53. Y. Yin, H. Sone, S. Hosaka, *J. Appl. Phys.* **102**, 064503 (2007)
54. M. Chen, K.A. Rubin, R.W. Barton, *Appl. Phys. Lett.* **49**, 502 (1986)
55. S.W. Ryu, J.H. Oh, B.J. Choi, S.Y. Hwang, S.K. Hong, C.S. Hwang, H.J. Kim, *Electrochem. Solid-State Lett.* **9**, G259 (2006)
56. F. Rao, Z.T. Song, K. Ren, X.L. Zhou, Y. Cheng, L.C. Wu, B. Liu, *Nanotechnology* **22**, 145702 (2011)
57. T.H. Jeong, M.R. Kim, J.W. Park, C. Yeon, *Jpn. J. Appl. Phys.* **39**, 2775 (2000)
58. M.H.R. Lankhorst, L.V. Pieterson, M.V. Schijndel, B.A.J. Jacobs, J.C.N. Rijpers, *Jpn. J. Appl. Phys.* **42**, 863 (2003)
59. W.J. Wang, D. Loke, L.P. Shi, R. Zhao, H.X. Yang, L.T. Law, L.T. Ng, K.G. Lim, Y.C. Yeo, T.C. Chong, A.L. Lacaita, *Scientific Reports* **2**, 360 (2012)
60. D.H. Ahn, S.L. Cho, H. Horill, D.H. Im, I.S. Kim, G.H. Oh, S.O. Park, M.S. Kang, S.W. Nam, C.H. Chung, in *Proc. EPCOS*, (2010), pp. 87
61. M. Zhu, L.C. Wu, F. Rao, Z.T. Song, X.L. Ji, D.N. Yao, Y. Cheng, S.L. Lv, S.N. Song, B. Li, L. Xu, *Appl. Phys. Lett.* **114**, 124302 (2013)

Ti-Sb-Te Phase Change Materials: Component  
Optimisation, Mechanism and Applications

Zhu, M.

2017, XVI, 124 p. 83 illus., Hardcover

ISBN: 978-981-10-4381-9